ISSN 1063-7834, Physics of the Solid State, 2015, Vol. 57, No. 4, pp. 752–759. © Pleiades Publishing, Ltd., 2015.
Original Russian Text © T.S. Argunova, M.Yu. Gutkin, V.G. Kohn, E.N. Mokhov, 2015, published in Fizika Tverdogo Tela, 2015, Vol. 57, No. 4, pp. 733–740.

MECHANICAL PROPERTIES, PHYSICS OF STRENGTH, AND PLASTICITY

Mechanisms of the Formation of Morphological Features of Micropipes in Bulk Crystals of Silicon Carbide

T. S. Argunova[a, *], M. Yu. Gutkin[b, c, d], V. G. Kohn[e], and E. N. Mokhov[a]

[a] *Ioffe Physical-Technical Institute, Russian Academy of Sciences, Politekhnicheskaya ul. 26, St. Petersburg, 194021 Russia*
** e-mail: argunova2002@mail.ru*
[b] *Institute of Problems of Mechanical Engineering, Russian Academy of Sciences, Bolshoi pr. 61, St. Petersburg, 199178 Russia*
[c] *St. Petersburg State Polytechnical University, Politekhnicheskaya ul. 29, St. Petersburg, 195251 Russia*
[d] *Saint Petersburg State University of Information Technologies, Mechanics and Optics, Kronverkskii pr. 49, St. Petersburg, 197101 Russia*
[e] *National Research Centre "Kurchatov Institute," pl. Akademika Kurchatova 1, Moscow, 123182 Russia*

Received October 16, 2014

Abstract—New morphological features of dislocation micropipes in silicon carbide single crystals have been investigated experimentally and theoretically. It has been shown that the cylindrical shape of micropipes is unstable, and the cross-sectional sizes of the micropipes change along their axes. The experimental results have been obtained by measuring X-ray phase-contrast microscopy images of micropipes in highly coherent synchrotron radiation. The cross-sectional sizes of the micropipes have been determined using computer simulation of their images. A theoretical model of the transformation of dislocations into micropipes due to nonequilibrium processes of pipe diffusion and coagulation of vacancies on dislocations parallel to the crystal growth axis has been proposed.

DOI: 10.1134/S1063783415040058

1. INTRODUCTION

Hexagonal silicon carbide (SiC) is a promising material for use in the design and fabrication of power semiconductor devices. Owing to the improvement of production technologies for SiC ingots of large diameter, the use of this material is gradually becoming one of the main directions in the development of high-current electronics. In recent years, the diameter of commercial SiC single crystals has been increased from 50 to 100–150 mm, while the density of defects has been decreased by several orders of magnitude.

In particular, the density of micropores threading over the entire length of the ingot has been decreased to less than 1 cm^{-2} [1]. These pores in the form of pipes, as has been commonly believed, are formed on superdislocations with large Burgers vectors. The model of a superdislocation with a hollow core was proposed in the middle of the last century by Frank [2]. Based on the energy minimization condition for a screw dislocation with Burgers vector b and a hollow core with radius r_0, Frank derived the linear relationship between r_0 and b^2: $r_0 = (Gb^2)/8\pi^2\gamma$, where G is the shear modulus of the crystal in the isotropic approximation and γ is the specific free surface energy of the crystal. The validity of this formula was experimentally confirmed in a number of studies. Using the dislocation core radius r_0 measured by scanning electron microscopy (SEM) [3] or atomic force microscopy (AFM) [4–7] and the Burgers vector measured by the methods of AFM [4, 5], synchrotron radiation topography [3], transmission electron microscopy (TEM) [6], or polarized light microscopy [8], the authors of [3–6, 8] plotted the dependence $r_0 \sim b^2$ and determined the surface energy γ of the crystal. However, for the shear modulus $G = 200$ GPa, the values of γ obtained in these works differed significantly: $\gamma = 4.0$, 0.20, 0.14, 0.79, 0.93, and 2.0 J/m^2 for $r_0 = 0.09$–0.16, 0.05–2.10, 0.025–6.0, 0.1–6.0, and 0.05–0.90 μm, respectively.

The results obtained from investigations of the characteristics of micropipes were used in the development of different models of their formation. Strunk et al. [6] proposed a model for the formation of mixed-type superdislocations on pileups of partial dislocations. Other researchers gave evidence in favor of the fact that hollow cores are typical of screw-type dislocations [9], which can nucleate in inclusions of the second phase [10] or in the process of association of nuclei in the initial stage of the crystal growth [7]. Each model offered its own answer to the question as to why single dislocations (with $b = 1c$, where c is the lattice parameter of the SiC crystal) with Burgers vectors of the same sign are attracted to each other to form a superdislocation. The reasons were considered to be reactions occurring in regions of dense dislocation

pileups—near the boundaries of misoriented domains [11], inclusions of other polytypes [5, 12], and clusters of stacking faults [6],—as well as effects of repulsion between the spiral growth steps on a growing surface [12].

The progress made in the production of high-quality crystals has confirmed the validity of the aforementioned models. A decrease in the number of second-phase inclusions, a decrease in the density of defect boundaries, and an increase in the quality of the crystal structure at the initial stage of the growth led to a substantial decrease in the density of micropipes and, in some cases, even to their absence in the material [1]. However, there is a reason to believe that not all the known features of the formation of micropipes have already found the explanation, and a successful elimination of these defects requires further investigation.

First, the large difference in surface energies γ obtained by different authors suggests that the formation of micropipes is determined, to a large extent, by the kinetics of nucleation and interaction of defects rather than by the Frank thermodynamics. In a relatively early paper by Augustine et al. [13], it was noted that dislocations can transform into micropipes under the influence of changes in the growth conditions, in particular, temperature and pressure, which can induce the migration of point defects over dislocation cores. At present, it has been established that the kinetic processes of overgrowing of micropipes can be explained by the diffusion outflow of vacancies from a micropipe [14].

Second, experimental evidence in support of each of the aforementioned models was obtained by methods with different restrictions. The surface-sensitive SEM and AFM methods can reveal growth pits and spirals in places where micropipes outcrop on the growth surface. However, the shape of a growth pit does not reflect the shape of a micropipe over the entire path of its propagation in the bulk of the crystal. The optical microscopy technique cannot resolve fine details of the morphology of small micropipes. The TEM method, on the contrary, has a very high resolution for images of micropipes with a radius of a few microns, which are distributed with a low density. The X-ray topography and polarized light microscopy techniques do not reveal the shape of a micropipe. Currently, only the X-ray phase contrast, which can be observed on synchrotron radiation sources under conditions of high spatial coherence, makes it possible to investigate the sizes and shape of micropipes in the bulk of the crystals [15]. A combination of X-ray phase contrast with topography in a synchrotron radiation beam provides the most comprehensive information about these defects [16].

Finally, it is known that the removal of the causes of micropipe nucleation does not always lead to the overgrowing of the micropipe itself. In particular, inclusions of other polytypes [17, 18] and slit-shaped pores formed along their boundaries [19, 20] are overgrown according to the mechanisms considered, for example, in [16]. However, dislocations generated by inclusions can transform into micropipes that are persistently overgrowing throughout the rest of the length of the ingot. Until now, it was thought that single dislocations generated by elastic stresses at the boundaries of polytypes form superdislocations due to the reactions [5, 12] and micropipes according to the Frank model [2].

Using the technique of X-ray phase-contrast microscopy in combination with computer simulation of images, in this work we investigated micropipes at the boundaries of inclusions of other polytypes. It turned out that, contrary to the Frank model, they can have not only a circular cross section but also an elliptical cross section whose sizes change along the micropipe axis. These and other interesting features of the formation of micropipes will be explained below in the framework of a new model of the formation of micropipes through the pipe diffusion and coagulation of vacancies on the dislocation cores.

2. EXPERIMENTAL TECHNIQUE

The X-ray phase-contrast images are formed as a result of the diffraction of synchrotron radiation by a sample containing electron density fluctuations, for example, micropores. Locally changing the phase of the incident plane wave, inhomogeneities form a diffraction pattern, which can be recorded in both the near and far fields, i.e., either in the form of a contour image or as the interference of a wave scattered by defects with unperturbed radiation [21]. The incident radiation should be coherent. The spatial coherency is determined by the quantity $\alpha = S/z_0$, where S is the transverse size of the source and z_0 is the distance from the source to the sample. The temporal coherence in the absence of a monochromator is determined by the width of the synchrotron radiation spectrum, which is caused by the electron energy. In the high-energy range, the intensity of synchrotron radiation naturally decreases with an increase in the energy. In the low-energy range, the radiation is absorbed by all objects encountered in the path of the beam, including the sample. This results in the formation of a spectral peak with the maximum at an energy E and a half-width ΔE. The X-ray imaging experiments were performed using synchrotron radiation from the 6D X-ray micro-imaging beamline at the Pohang Light Source (Pohang, South Korea). The bending magnet provided the vertical size of the focus $S = 60$ μm at the distance $z_0 = 32$ m from the sample. In this case, the spatial coherence length was $T_s = \lambda/\alpha = 42$ μm, which significantly exceeded the diameter of conventional micropipes in SiC (up to 10 μm). For SiC wafers with a thickness of ~500 μm, the spectral peak with the half-width $\Delta E = 24$ keV ($\Delta\lambda = 0.52$ Å) had a maximum at $E = 16$ keV ($\lambda = 0.775$ Å), and the temporal coherence length T_t was 1.2 Å [15, 22].

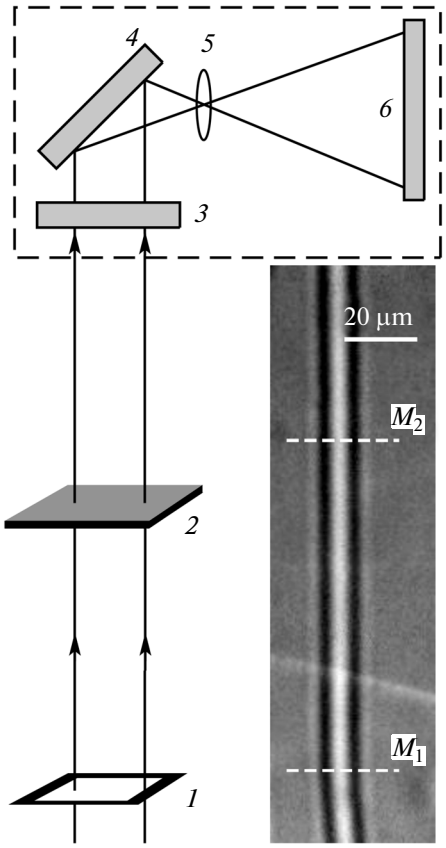

Fig. 1. Schematic diagram of the experiment: (*1*) entrance slit, (*2*) sample (SiC plate), (*3*) scintillation crystal, (*4*) mirror, (*5*) optical lens, and (*6*) detector. Arrows indicate the direction of the synchrotron radiation beam. The inset shows a the phase-contrast image of the micropipe.

The schematic diagram of the measurements is shown in Fig. 1. Slit *1* generates an X-ray beam of specified size. The beam passes through sample *2*, behind which interference images of micropipes arise. These images are recorded on a phase-contrast microscope consisting of elements located inside the rectangle drawn by the dashed line. Scintillation crystal *3* converts the diffracted radiation into the visible light. The radiation from the scintillation crystal is directed by mirror *4* into optical lens *5*, which forms an image on detector array *6*. The lens cannot increase the resolution of the interference pattern. However, increasing the size of the interference pattern to the size of the visual field of the detector, it effectively decreases the size of the pixel. For example, if the detector has a resolution of 3296 × 2472 pixels and a pixel size of 5.5 × 5.5 μm, the optical magnification 20× makes the visual field of the detector equal to 906 × 680 μm, thus effectively decreasing the pixel size to 0.275 μm.

The profiles of the relative intensity distributions were measured across the images of micropipes with the use of the ImageJ program. The cross-sectional diameters of the micropipes were calculated using the FIMTIM (Fit Micro-Tube Image) program [15, 23]. This program was developed for numerical calculations of the intensity profiles for monochromatic synchrotron radiation harmonics on a grid of points in the range from 5 to 40 keV with their subsequent summation taking into account the actual spectrum [15] and absorption. The diameters of the micropipe elliptical cross sections D and D_0 (across and along the synchrotron radiation beam, respectively) were determined automatically from the condition that the theoretical and experimental intensity profiles coincide with each other. In order to estimate the accuracy of the result, the program calculated the dependence of the quantity $\chi^2 - \chi^2_{\min}$, where $\chi^2_{\min}$ is the minimum sum of the squared deviations, on the desired parameters D and D_0 and plotted the map $\chi^2(D, D_0) - \chi^2_{\min}$ in the vicinity of the minimum point [22].

The SiC wafers were prepared from a 4*H*-polytype crystal grown by sublimation [17]. The crystal growth occurred at a temperature of 2100°C in an argon atmosphere at a rate of 350 μm/h. The crystal contained layered inclusions of the 6*H* polytype. The 6*H*-SiC layers aligned parallel to the (0001) plane were located approximately in the middle of the 4*H*-SiC ingot and had a small thickness along the [0001] growth axis. The surface of the sample cut parallel to the growth axis crossed the boundaries of inclusions. According to the data of optical microscopy (not presented in the paper), there were no micropipes in the region between the seed and the boundaries of the inclusions. They were formed near the inclusions, as noted, for example, in [12, 16], and propagated up to the free surface of the crystal. Before measuring the images, the surface of the samples was carefully polished to remove the damaged layer and roughness. During the measurements, the samples were located perpendicular to the beam so that the micropipe axes had the horizontal direction. In this case, the spatial coherence was determined by the minimum size of the source in the vertical direction: $S = 60$ μm.

3. EXPERIMENTAL RESULTS

The inset in Fig. 1 shows a phase-contrast image of the micropipe located perpendicular to the synchrotron radiation beam. The image was obtained in the far field, because the diameter of the first Fresnel zone $2r_1 = 2(\lambda z_1)^{1/2} = 11$ μm (where $\lambda = 0.775$ Å and the distance from the detector to the sample $z_1 = 40$ cm) is larger than the diameters of the micropipes [3, 5, 6, 8]. It has the form of a universal averaged intensity profile [24], which consists of the central peak and strongly weakened lateral oscillations having a minimum and a maximum. The distance between the oscillations seems to be constant along the micropipe axis. It may seem that the cross-sectional size is equal to the size of the central bright band between two dark bands. How-

ever, this size is equal to the diameter of the first Fresnel zone. The true diameters of the micropipe in the far field are manifested only through the contrast, and their determination requires the computer simulation of the image.

The experimental profiles of the relative intensity distributions were measured at two levels along the micropipe axis: M_1 and M_2. Since the far-field image is determined entirely by the first Fresnel zone, changes in the shape and sizes of the cross section affect the structure of the image not only across but also along the axis within $2r_1$. No matter how abrupt jumps in the diameter can be, they cannot be found by fitting the one-dimensional cross sections when the distance between the levels is less than $2r_1$. Hence, the distance between the levels M_1 and M_2 was chosen deliberately larger: $8.2r_1 = 90$ μm.

Using the FIMTIM program, we determined the diameters D and D_0 by comparing the calculated and experimental intensity profiles. The results of the calculations for the M_1 level are presented in Fig. 2. Symbols in Fig. 2a depict the normalized experimental curve, which for $\chi^2_{min} = 7.745 \times 10^{-5}$ coincides with the theoretical curve (solid line). In this case, the micropipe has the following cross-sectional diameters: $D = 1.76$ μm and $D_0 = 1.52$ μm. Figure 2b shows the map of the distribution $\chi^2(D, D_0) - \chi^2_{min}$ in the vicinity of the minimum point. The black and white colors on this map correspond to $\chi^2_{min} = 7.824 \times 10^{-5}$ and $\chi^2_{max} = 9.290 \times 10^{-5}$, respectively. All values of $\chi^2 > \chi^2_{max}$ were replaced by χ^2_{max}. The region of small values χ^2 has the form of an approximately symmetrical hyperbole with the minimum size along the direction $D = D_0$ and with the maximum size in the perpendicular direction. The absence of localization in the region of the minimum reflects a specific feature of the far-field images of micropipes: a change in the cross-sectional sizes of the micropipe does not lead to a change in the size of its image and affects only the contrast scaled by the cross-sectional area [24]. By multiplying D and D_0, we obtain the cross-sectional area at the M_1 level: $\sigma_1 = \pi D D_0 = 8.4$ μm^2. The small distortion of the symmetry of the map along the axes D and D_0 ($D/D_0 = 1.2$) shows that the cross section has a slightly oval shape.

It is interesting to note that, for the M_2 level, the program gave quite different values of the cross-sectional diameters: $D = 2.54$ μm and $D_0 = 1.18$ μm. The region of the minimum that corresponds to this level is shown in Fig. 2c. It can be seen now that the hyperbolic distribution of quantities χ^2 is significantly more extended along the axis of the transverse diameter D, which indicates an increase in the ellipticity of the cross section: $D/D_0 = 2.2$. By multiplying the new values of the cross-sectional diameters, we obtain the cross-sectional area at the M_2 level: $\sigma_2 = 9.4$ μm^2.

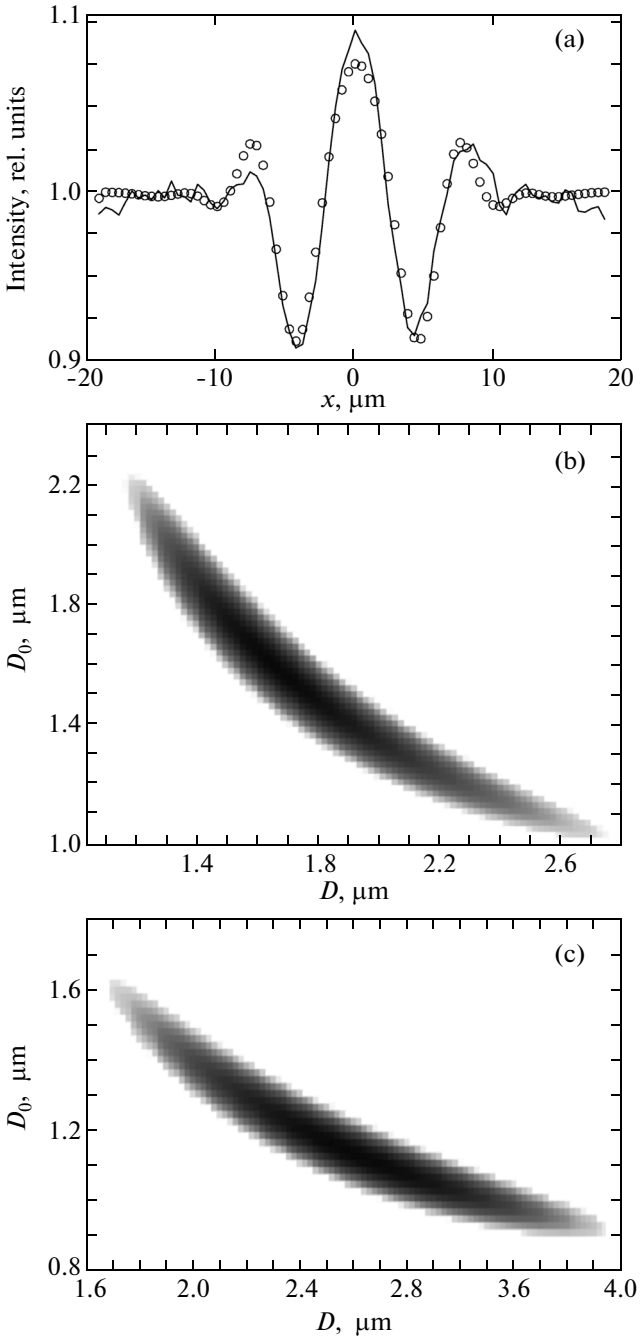

Fig. 2. Results of the computer simulation of the micropipe image shown in Fig. 1. (a) Experimental (symbols) and calculated (solid line) profiles of the relative intensity at the M_1 level, which coincide with the best accuracy of $\chi^2_{min} = 7.745 \times 10^{-5}$. (b, c) Maps of the distribution of the minimum sum of the squared deviations $\chi^2 - \chi^2_{min}$ for different desired parameters D and D_0 in the vicinity of the minimum point at the levels M_1 and M_2.

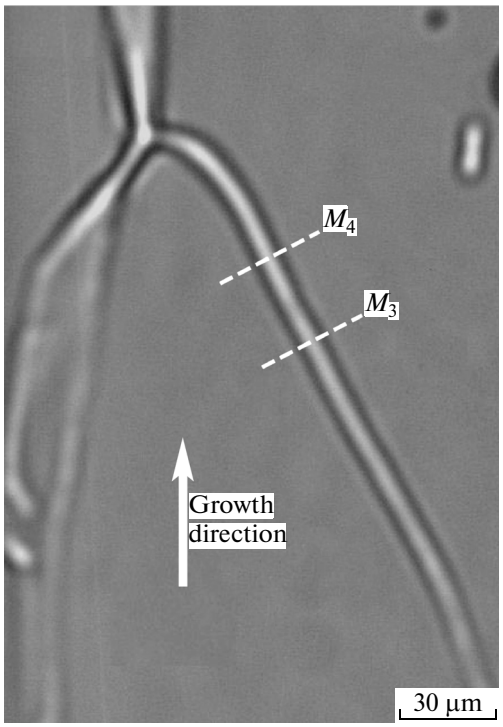

Fig. 3. Image of the inclined micropipe. The simulation of the intensity profiles was performed for the levels M_3 and M_4. The arrow indicates the direction of the crystal growth.

The micropipe shown in Fig. 1 is parallel to the crystal growth axis. However, some other micropipes deviated from the growth axis by rather large angles. The image of one of the inclined micropipes is shown in Fig. 3. Generally speaking, for inclined micropipes, the parameters of their cross sections by a synchrotron radiation beam are not equal to the true values of the cross-sectional diameters. Let us assume that the micropipe shown in Fig. 3 has a circular cross section with a diameter $2r_0$. It is also assumed that the micropipe axis forms an angle ψ with the vertical direction parallel to the crystal growth axis and does not have inclination angles with respect to the other axes. The parameters D and D_0, which were calculated with the FIMTIM program from the intensity profiles measured perpendicular to the crystal growth axis (Fig. 3), are related to the true diameter $2r_0$ by the expressions $D = 2r_0/\sin\psi$ and $D_0 = 2r_0$, where $D > D_0$. At the same time, the intensity profile can be measured across the micropipe axis if the image shown in Fig. 3 is clockwise rotated by the angle ψ. In this case, the FIMTIM program will calculate the correct values of the cross-sectional diameters. However, it should be kept in mind that the rotation of the micropipe image affects the accuracy in the determination of these diameters. The program takes into account the size of the source in accordance with the minimum (vertical) projection of the focus S, and the rotation angle ψ increases the size by an unknown value.

Parameters of the micropipes: diameters D and D_0 (across and along the synchrotron radiation beam, respectively) and cross-sectional area σ at the levels M_i ($i = 1$–4), determined using the FIMTIM program up to $\chi^2_{\min}$

M_i	D, μm	D_0, μm	σ, μm^2	$\chi^2_{\min}$
M_1	1.76	1.52	8.4	7.744×10^{-5}
M_2	2.54	1.18	9.4	7.295×10^{-5}
M_3	1.96	1.84	11.3	8.996×10^{-5}
M_4	5.32	1.32	22.0	4.501×10^{-5}

The intensity profiles were measured across the inclined micropipe by rotating the image with the ImageJ program. The distance between the levels was small, i.e., $2.6r_1 = 29$ μm, but large enough to ensure that the program would respond to changes in the cross section. According to the simulation data obtained at the M_3 level, the inclined micropipe has an approximately circular cross section: $D = 1.96$ μm and $D_0 = 1.84$ μm; $D/D_0 = 1.06$. However, at the M_4 level, the cross section becomes substantially elliptical: $D = 5.32$ μm and $D_0 = 1.32$ μm; $D/D_0 = 4.03$. The cross-sectional areas at the levels M_3 and M_4 are equal to $\sigma_3 = 11.3$ μm^2 and $\sigma_4 = 22.0$ μm^2, respectively.

The micropipe parameters obtained from the computer simulations are presented in the table. After studying many other micropipes in the 4*H*-SiC crystal and other such crystals, as well as in 6*H*-SiC crystals with 4*H*- and 15*R*-polytype inclusions, we came to the conclusion that many micropipes have the morphological features described above. First, the cross-sectional sizes of the micropipes change along their axes. Second, many micropipes are characterized by deviations from the cylindrical shape, which is characteristic of the cavity around the core of the screw superdislocation. Third, the cylindrical shape of some micropipes is unstable and can turn into an elliptical shape. Fourth, the micropipes have local curvatures. Finally, they can suddenly break down in the crystal. These features cannot be explained in the framework of the already known models for the formation of micropipes [6, 7, 10, 12]. In the next section, we will discuss the reasons for the deviation of the shape of micropipes from the equilibrium cylindrical shape predicted by Frank [2] and propose the vacancy mechanism of the formation of nonequilibrium micropipes.

4. DISCUSSION OF THE RESULTS

One of the possible scenarios for the formation of micropipes with a variable cross section suggests that the leading role belongs to the coagulation of vacancies and the scenario itself includes the following main stages: (1) the heterogeneous formation of disloca-

tions that are extended along the c axis and reach the front of crystal growth; (2) the pipe diffusion of vacancies from the surface deep into the crystal over the cores of these dislocations; (3) the coagulation of these vacancies around the dislocations; and (4) formation of a continuous cavity (micropipe) around the dislocations and the flattening of the surface of this micropipe through the surface diffusion of vacancies. The diffusion, coagulation, and subsequent absorption–emission of vacancies by the micropipe are strongly nonequilibrium processes, so that the formation of micropipes is determined, to a large extent, by the kinetics of their occurrence rather than by the Frank thermodynamics [2].

Now, we discuss how this scheme can explain the formation of micropipes with an oblate cross section. Let us consider not one dislocation, as before, but a few dislocations generated at the same stress concentrator (a large surface step, a pore, a foreign inclusion, an inclusion of another polytype, etc.). In the simplest case, it can be a dislocation dipole (Fig. 4a) or a pair of dislocations of the same sign (Fig. 4b). If these dislocations are located not too far from each other, then during the coagulation of vacancies, the formed pore can trap both dislocations simultaneously and acquires a cross section extended in the direction from one dislocation to the other dislocation. The divergence or convergence of dislocations during the crystal growth will cause the corresponding changes in the cross section of this "oblate" micropipe, and the deviations of dislocations in the directions at an angle to the imaginary line connecting them or, even more, the twisting of dislocations around the common axis will be perceived as a twisting of the "oblate" micropipe.

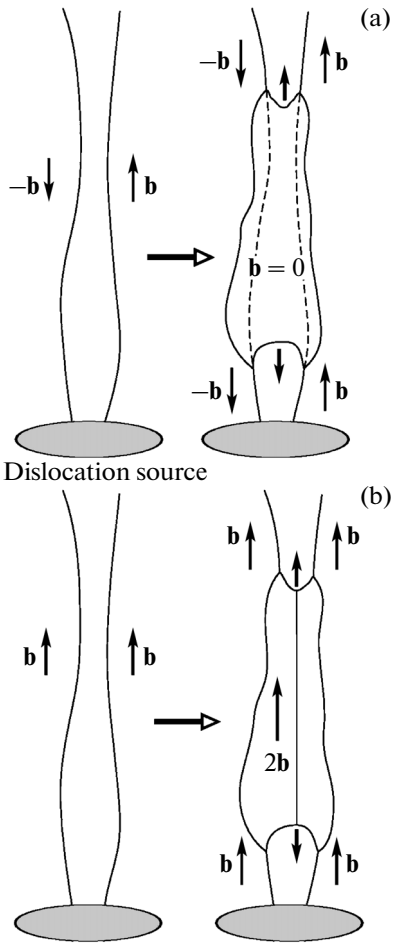

Fig. 4. Schematic diagram of the formation of an oblate micropipe on (a) dislocation dipole and (b) pair of dislocations of the same sign. Thick black arrows indicate the direction of the growth of the micropipe along the dislocation lines due to the absorption and surface diffusion of vacancies.

We estimate the conditions under which the formation of oblate micropipes will be energetically favorable. For a dislocation dipole, the coverage of both dislocations by the micropipe has the obvious advantage that, in this case, the annihilation of dislocations occurs within the micropipe and the dislocation dipole transforms into two dislocation half-loops, namely, the "upper" and "lower" half-loops (in these half-loops, the dislocations with Burgers vectors **b** and –**b** are bound to each other through the steps on the "upper" and "lower" surfaces of the micropipe, respectively). This gives a gain in the elastic energy of dislocations and in the energy of their cores. At the same time, an increase in the micropipe volume, which is required to cover the entire dipole, leads to an increase in the free surface energy of the micropipe, i.e., to a loss in the total energy of the system. The balance between the gain and loss of the total energy determines the critical size of the micropipe which cannot be exceeded. In the initial state (before the formation of a micropipe), the total energy of the dislocation dipole can be estimated as $W_1 = Gb^2/(2\pi)[\ln(d/r_c) + 2Z]$, where G is the shear modulus, b is the absolute value of the Burgers vector of the dislocation, d is the arm of the dislocation dipole, r_c is the cutoff radius of the elastic field of the dislocation at the dislocation core, and $Z \sim 1$ is the dimensionless parameter characterizing the energy of the dislocation core. After the formation of a micropipe and the annihilation of a dipole, the energy of the system (per unit length of the disappeared dislocations) can be estimated as $W_2 = \gamma L$, where L is the average perimeter of the cross section of the micropipe. The formation of such micropipe is energetically favorable for the change in the energy of the system $\Delta W = W_2 - W_1 = \gamma L - Gb^2/(2\pi)[\ln(d/r_c) + 2Z] < 0$, from which we immediately obtain the estimate for the critical perimeter L_c such that $L < L_c = Gb^2/(2\pi\gamma)[\ln(d/r_c) + 2Z]$.

The dependence of the energy change ΔW on the arm of the dislocation dipole d is shown in Fig. 5 for the following parameters of 4H-SiC: $c = 1$ nm, $G = 165$ GPa, and $\gamma = 0.2$ J/m^2 [3]. The curves were plotted

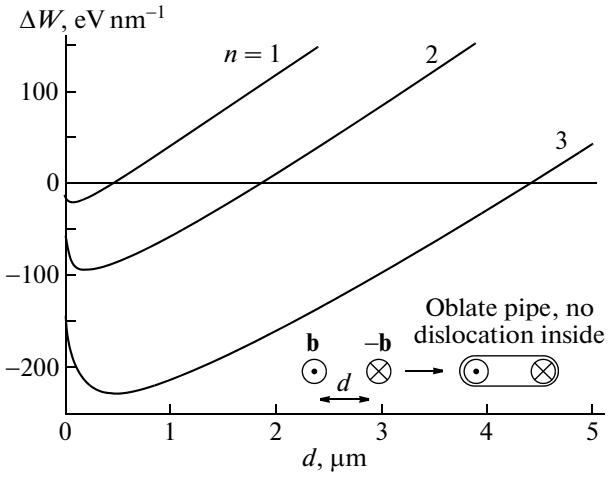

Fig. 5. Dependences of the energy change ΔW on the arm of the dislocation dipole d at $b = nc$ ($n = 1$, 2, and 3) for the parameters $c = 1$ nm, $G = 165$ GPa, $\gamma = 0.2$ J m^{-2}, and $\eta = 2.5$. The inset shows the scheme of the annihilation of the dipole upon the formation of an oblate micropipe around it.

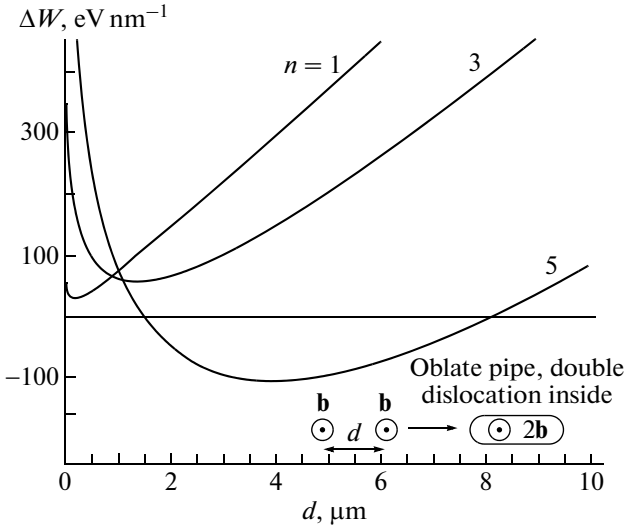

Fig. 6. Dependences of the energy change ΔW on the distance between dislocations d at $b = nc$ ($n = 1$, 3, and 5) for the parameters $c = 1$ nm, $G = 165$ GPa, $\gamma = 0.2$ J m^{-2}, and $\eta = 2.5$. The inset shows the scheme of the association of dislocations upon the formation of an oblate micropipe around them.

for three values of the Burgers vector $b = nc$ for $n = 1$, 2, or 3 with the cutoff parameter $r_c = b$. In the calculations, the cross-sectional perimeter L of the micropipe was assumed to be proportional to the dipole arm d, i.e., $L = \eta d$ for $\eta = 2.5$ (the lowest value of $\eta \sim 2$ corresponds to a flat slit, while the highest value of $\eta = \pi$ corresponds to a circle). As can be seen from Fig. 5, the maximum gain in the energy is achieved for $d \sim$ 0.07, 0.21, and 0.47 μm for $n = 1$, 2, and 3, respectively. At the same time, the formation of a micropipe remains energetically favorable for significantly higher values of the dipole arm $d < d_c = L_c/2.5 \sim 0.40$, 1.82, and 4.40 μm for $n = 1$, 2, and 3, respectively. These cross-sectional sizes of oblate micropipes are often observed in the experiment.

In the case of the formation of an oblate micropipe around a pair of dislocations of the same sign, we have $W_1 = Gb^2/(2\pi)[\ln\{R^2/(dr_c)\} + 2Z]$ and $W_2 \approx \gamma L + 2Gb^2/\pi\ln(2R/d)$, which gives the energy change $\Delta W = W_2 - W_1 = \gamma L + Gb^2/(2\pi)[\ln(16R^2r_c/d^3) - 2Z]$. Here, R is the cutoff parameter of the long-range elastic field of a paired dislocation, which can be taken as half of the distance between the dislocations of opposite signs in the sample. In the numerical calculations, we used $R = 10$ μm, which corresponds to the dislocation density of $\sim 10^6$ cm^{-2}, which is characteristic of the boundaries of inclusions of other polytypes. The dependence of the energy change ΔW on the distance between the dislocations d is shown in Fig. 6 for the same parameters as for the curves in Fig. 5. The curves shown in Fig. 6 are plotted for three values of the Burgers vector $b = nc$ for $n = 1$, 3, and 5. As can be seen from Fig. 6, the formation of an oblate micropipe around the pair of dislocations with the Burgers vectors equal $1c$ and $3c$ is energetically unfavorable. In order for such micropipe to be formed, it is necessary that the absolute value of the Burgers vector would be no less than $5c$. For $b = 5c$, the micropipe size can vary from approximately 1.5 to 8.2 μm, and the maximum gain in the energy corresponds to $d \approx 4$ μm. Therefore, in contrast to the previous case of a dislocation dipole, when the formation of an oblate micropipe is energetically favorable for any value of the Burgers vector and $d < d_c$, here, we have two critical conditions for the formation of an oblate micropipe: $b \geq b_c = 5c$ and $d_{c1} < d < d_{c2}$. The range of permissible values d is determined by the Burgers vector: the higher is the absolute value of the Burgers vector, the wider is the range permissible distances d.

Thus, the formation of oblate micropipes can be explained by the fact that they cover several dislocations (a bundle of dislocations), thus minimizing their own surfaces. In this case, the largest cross-sectional size of the micropipe approximately corresponds to the distance between the farthest dislocations in the bundle. If the bundle of dislocations is a self-screened ensemble of dislocations, from a dipole to an arbitrary multipole, then the driving force of the coverage of the whole bundle by a micropipe is the possibility of the annihilation of the bundle inside the micropipe, with the main limitation that the bundle size cannot exceed a critical size d_c. If the dislocation bundle consists of dislocations of the same sign (or of different signs, but the number of dislocations of the same sign differs from the number of dislocations of the opposite sign), then the driving force of the coverage of the bundle by a micropipe is the decrease in the density of elastic energy near the bundle, with the following main limi-

tations: (i) the Burgers vectors of the (uncompensated) dislocations exceed the critical value b_c, and (ii) the bundle size (the distance between the uncompensated dislocations) lies in the range between the two critical values d_{c1} and d_{c2}, which is determined by the Burgers vector b. Numerical estimates of the critical values d_c, d_{c1}, and d_{c2} are in good agreement with the sizes of oblate micropipes observed in our experiment.

5. CONCLUSIONS

The X-ray phase-contrast microscopy technique used in this work made it possible to observe the shape of micropipes over the entire path of their propagation in the bulk of the crystal. The sizes and cross sections of micropipes were determined using the computer simulation of their phase-contrast images. By simulating phase-contrast images of a large number of micropipes in 4*H*- and 6*H*-SiC crystals, we revealed new morphological features that were not explained in the framework of well-known models: the instability of the diameter and cylindrical shape of the micropipes, local curvatures, etc. Reasoning from the fact that these features are caused by nonequilibrium processes, we proposed an alternative mechanism for the formation of micropipes in a growing SiC crystal. The leading role in this mechanism belongs to the coagulation of vacancies around dislocations that are located along the *c* axis and reach the front of the crystal growth. Numerical estimates of the critical parameters responsible for the formation of oval cavities around bundles of dislocations are in good agreement with the experimental data.

We investigated inclusions of other polytypes as a source of dislocation nucleation. However, these processes will occur near dislocation pileups caused by other sources. The formation of nonequilibrium micropipes can be avoided by decreasing the inhomogeneity in the distribution of dislocations, as well as by decreasing their density.

The previously unknown morphological features of the micropipes were revealed only owing to the quantitative approach to the processing of phase-contrast images. This approach opens up new possibilities for studying other structurally heterogeneous materials, for example, AlN and GaN.

ACKNOWLEDGMENTS

M.Yu. Gutkin acknowledges the support of the Russian Science Foundation (project no. 14-29-00086) and E.N. Mokhov acknowledges the support of the Russian Foundation for Basic Research (project no. 13-02-00802).

REFERENCES

1. C. R. Eddy and D. K. Gaskill, Jr., Science (Washington) **324**, 1398 (2009).
2. F. C. Frank, Acta Crystallogr. **4**, 497 (1951).
3. W. Si, M. Dudley, R. Glass, V. Tsvetkov, and C. Carter, J. Electron. Mater. **26**, 128 (1997).
4. J. Giocondi, G. S. Rohrer, M. Skowronski, V. Balakrishna, G. Augustine, H. M. Hobgood, and R. H. Hopkins, Mater. Res. Soc. Symp. Proc. **423**, 539 (1996).
5. J. Heindl, W. Dorsch, R. Eckstein, D. Hofmann, T. Marek, St. G. Müller, H. P. Strunk, and A. Winnacker, J. Cryst. Growth **179**, 510 (1997).
6. H. P. Strunk, W. Dorsch, and J. Heindl, Adv. Eng. Mater. **2**, 386 (2000).
7. X. Ma, J. Appl. Phys. **99**, 063513 (2006).
8. X. Ma, Mater. Sci. Eng., B **129**, 216 (2006).
9. X. R. Huang, M. Dudley, W. M. Vetter, W. Huang, S. Wang, and C. H. Carter, Jr., Appl. Phys. Lett. **74**, 353 (1999).
10. M. Dudley, X. R. Huang, W. Huang, A. Powell, S. Wang, P. Neudeck, and M. Skowronski, Appl. Phys. Lett. **75**, 784 (1999).
11. P. Pirouz, Philos. Mag. A **78**, 727 (1998).
12. N. Ohtani, M. Katsuno, T. Fujimoto, T. Aigo, and H. Yashiro, J. Cryst. Growth **226**, 254 (2001).
13. G. Augustine, McD. Hobgood, V. Balakrishna, G. Dunne, and R. H. Hopkins, Phys. Status Solidi B **202**, 137 (1997).
14. S. Yu. Davydov and A. A. Lebedev, Semiconductors **45** (6), 727 (2011).
15. V. G. Kohn, T. S. Argunova, and J. H. Je, Appl. Phys. Lett. **91**, 171901 (2007).
16. T. S. Argunova, M. Yu. Gutkin, J. H. Je, V. G. Kohn, and E. N. Mokhov, in *Physics and Technology of Silicon Carbide Devices*, Ed. by Y. Hijikata (InTech, Rijeka, Croatia, 2013), Chap. 2, p. 27.
17. Yu. A. Vodakov, A. D. Roenkov, M. G. Ramm, E. N. Mokhov, and Yu. N. Makarov, Phys. Status Solidi B **202**, 177 (1997).
18. N. Ohtani, M. Katsuno, H. Tsuge, T. Fujimoto, M. Nakabayashi, H. Yashiro, M. Sawamura, T. Aigo, and T. Hoshino, Microelectron. Eng. **83**, 142 (2006).
19. D. Siche, H.-J. Rost, J. Doerschel, D. Schulz, and J. Wollweber, J. Cryst. Growth **237–239**, 1187 (2002).
20. M. Yu. Gutkin, A. G. Sheinerman, M. A. Smirnov, T. S. Argunova, J. H. Je, S. S. Nagalyuk, and E. N. Mokhov, J. Appl. Phys. **106**, 123515 (2009).
21. M. Born and E. Wolf, *Principles of Optics*, 4th ed. (Pergamon, London, 1968), Chap. 10.
22. V. G. Kohn, T. S. Argunova, and J. H. Je, AIP Adv. **3**, 122109 (2013).
23. T. S. Argunova, V. G. Kohn, and J. H. Je, J. Surf. Invest. **2** (6), 861 (2008).
24. V. G. Kohn, T. S. Argunova, and J. H. Je, J. Surf. Invest. **5** (1), 1 (2011).

Translated by O. Borovik-Romanova